AGU PUBLICATIONS

JGR

Journal of Geophysical Research: Oceans

RESEARCH ARTICLE

10.1002/2015JC010697

Circulation of modified Circumpolar Deep Water and basal melt beneath the Amery Ice Shelf, East Antarctica

Laura Herraiz-Borreguero[1,2], Richard Coleman[2,3], Ian Allison[2], Stephen R. Rintoul[2,3,4], Mike Craven[2], and Guy D. Williams[2,3]

[1]Centre for Ice and Climate–Niels Bohr Institute, University of Copenhagen, Copenhagen, Denmark, [2]Antarctic Climate and Ecosystem Cooperative Research Centre, University of Tasmania, Hobart, Tas 7001, Australia, [3]Institute for Marine and Antarctic Studies, University of Tasmania, Hobart, Tas 7001, Australia, [4]CSIRO Wealth from Oceans National Research, Flagship and Centre for Australian Weather and Climate Research—A partnership of CSIRO and the Bureau of Meteorology, Hobart, Tasmania, Australia

Key Points:
- Modified CDW inflow (0.22 Sv) occurs from March to August
- mCDW causes a net basal melt rate of up to 2 ± 0.5 m/yr
- Heat content flux by mCDW shows high intra-annual variability (up to 40%)

Correspondence to:
L. Herraiz-Borreguero,
lherraiz@nbi.ku.dk

Citation:
Herraiz-Borreguero, L., R. Coleman, I. Allison, S. R. Rintoul, M. Craven, and G. D. Williams (2015), Circulation of modified Circumpolar Deep Water and basal melt beneath the Amery Ice Shelf, East Antarctica, *J. Geophys. Res. Oceans*, *120*, 3098–3112, doi:10.1002/2015JC010697.

Received 12 JAN 2015
Accepted 30 MAR 2015
Accepted article online 8 APR 2015
Published online 26 APR 2015

Abstract Antarctic ice sheet mass loss has been linked to an increase in oceanic heat supply, which enhances basal melt and thinning of ice shelves. Here we detail the interaction of modified Circumpolar Deep Water (mCDW) with the Amery Ice Shelf, the largest ice shelf in East Antarctica, and provide the first estimates of basal melting due to mCDW. We use subice shelf ocean observations from a borehole site (AM02) situated ~70 km inshore of the ice shelf front, together with open ocean observations in Prydz Bay. We find that mCDW transport into the cavity is about 0.22 ± 0.06 Sv (1 Sv = 10^6 m^3 s^{-1}). The inflow of mCDW drives a net basal melt rate of up to 2 ± 0.5 m yr^{-1} during 2001 (23.9 ± 6.52 Gt yr^{-1} from under about 12,800 km^2 of the north-eastern flank of the ice shelf). The heat content flux by mCDW at AM02 shows high intra-annual variability (up to 40%). Our results suggest two main modes of subice shelf circulation and basal melt regimes: (1) the "ice pump"/high salinity shelf water circulation, on the western flank and (2) the mCDW meltwater-driven circulation in conjunction with the "ice pump," on the eastern flank. These results highlight the sensitivity of the Amery's basal melting to changes in mCDW inflow. Improved understanding of such ice shelf-ocean interaction is crucial to refining projections of mass loss and associated sea level rise.

1. Introduction

Antarctic ice sheet mass loss has been linked to an increase in oceanic heat supply that enhances the basal melt and thinning of Antarctic ice shelves. The floating ice shelves buttress the outlet glaciers of the ice sheet [*Dupont and Alley*, 2005]. Collapse of ice shelves has been observed to trigger accelerated glacier discharge into the ocean, directly contributing to sea level rise [*Scambos et al.*, 2004; *Shepherd et al.*, 2010]. The recent widespread and intensifying glacier acceleration along the coastal margins of the Antarctic ice sheet [*Pritchard et al.*, 2012; *Rignot et al.*, 2013] underlines the need for better understanding of ice shelf-ocean interaction.

The rate of basal melt varies around Antarctica [*Depoorter et al.*, 2013], reflecting differences in ocean forcing [*Pritchard et al.*, 2012]. Lower melt rates under the large ice shelves result from the relatively low ocean heat content of cold shelf waters [*Pritchard et al.*, 2012]. The highest thinning rates occur where warm water, namely modified Circumpolar Deep Water (mCDW), enters the ice shelf cavities [*Pritchard et al.*, 2012]. This has been observed in the Amundsen [*Jacobs et al.*, 2011] and Bellingshausen [*Jenkins and Jacobs*, 2008] seas, in West Antarctica. In East Antarctica, the impact of mCDW is more ambiguous (i.e., mCDW is present, but less mCDW appears to reach the ice shelf cavities). However, the high melt rates beneath a number of smaller East Antarctic ice shelves reported recently [*Rignot et al.*, 2013] imply a previously undocumented strong ocean thermal forcing.

The Amery Ice Shelf (AIS; 60°E–70°E), with an area of ~62,000 km^2, is the third largest embayed ice shelf in Antarctica and the largest in East Antarctica (Figure 1). Although small compared with the Ross and the Filchner-Ronne ice shelves, the AIS is fed by the Lambert Glacier system, which drains ~16% of the area of East Antarctica [*Allison*, 1979]. Over the past decades, monitoring of the ocean underneath the AIS has been an important objective of the Amery Ice Shelf-Ocean Research (AMISOR) Project. While significant data sets

© 2015. American Geophysical Union. All Rights Reserved.

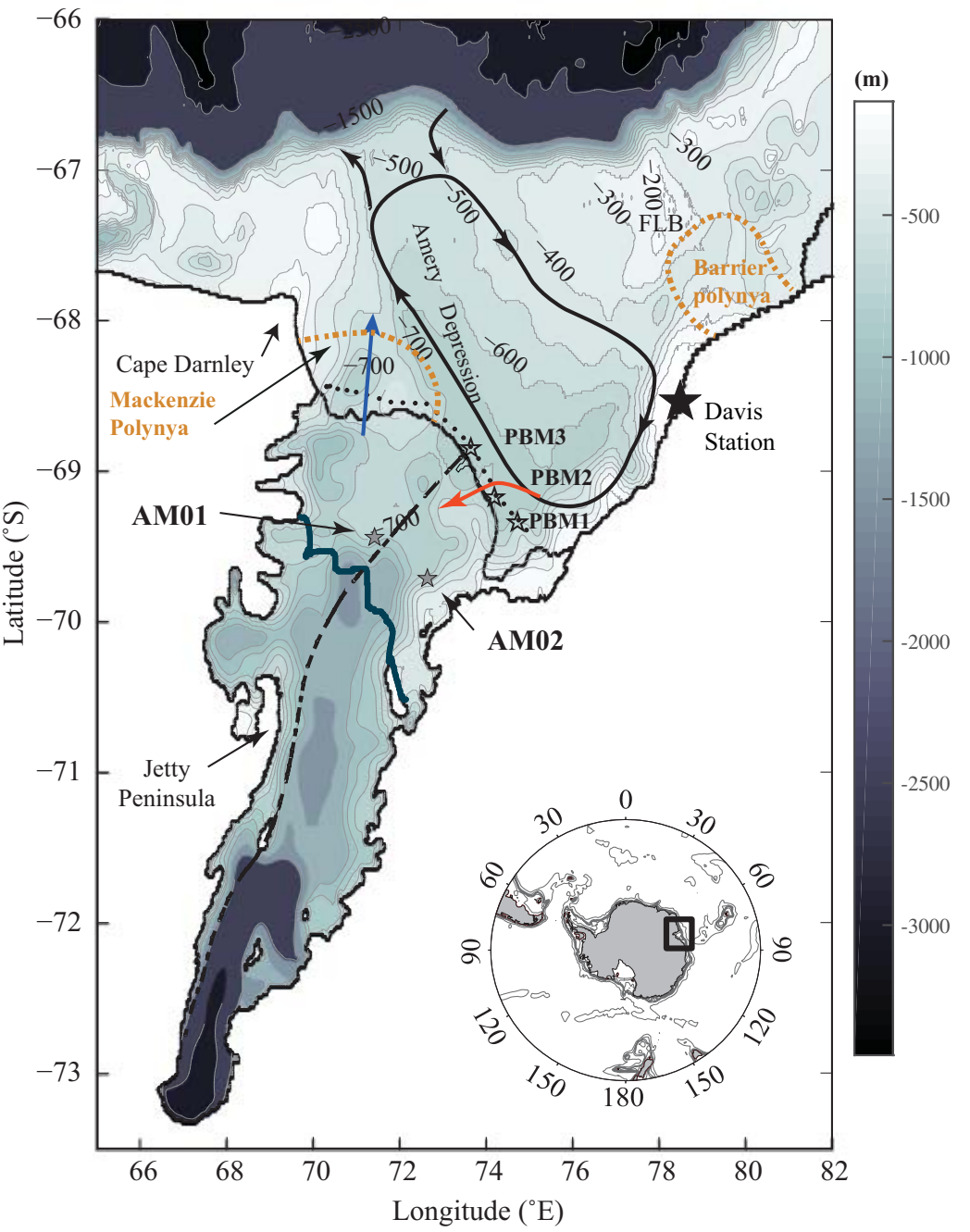

Figure 1. Amery Ice Shelf with borehole sites AM01 and AM02 (gray stars). Open ocean moorings PBM1–3 are shown as an empty star, and the 2001 ship hydrographic section is shown as black dots along the ice shelf front. The black-dashed line is the Fisher Glacier flow line [*Raup et al.*, 2005]. The gray thick line across the ice shelf is the 500 m ice shelf draft. The black thick line passing through AM02 is the 350 m water column thickness. Bathymetry is shown as background contours (bathymetry, ice shelf draft, and grounding line are from *Timmermann et al.* [2010]). FLB: Four Ladies Bank. The approximate location of the Mackenzie and Barrier polynyas are shown as an orange dashed line, following *Tamura et al.* [2008]. The blue and red arrows depict the outflow of ISW and the inflow of mCDW, respectively.

have been retrieved from beneath ice shelves in West Antarctica [e.g., *Clough and Hansen*, 1979; *Foster*, 1983; *Jacobs et al*., 1979; *Nicholls and Jenkins*, 1993], results from the AMISOR Project (2001–ongoing) comprise a comprehensive array of data (oceanographic moorings, sediment cores, glacial and marine ice samples, ocean currents, thermistors, and fiber-optic ice/ocean temperature measurements, in addition to a wide range of glaciological and geophysical measurements) for investigating ice shelf-ocean interactions.

The ocean circulation in Prydz Bay consists of a large cyclonic gyre, centered in a deep channel, known as the Amery Depression [*Nunes Vaz and Lennon*, 1996; *Smith et al*., 1984]. The gyre is associated with a relatively narrow coastal current that runs along the AIS calving front and continues westward after leaving Prydz Bay (Figure 1). Here the current becomes very strong, with currents along the western side of Prydz Bay exceeding 1 m s^{-1} [*Nunes Vaz and Lennon*, 1996]. Several regional studies have modeled the ocean circulation in Prydz Bay and beneath the AIS [e.g., *Williams et al*., 2001; *Galton-Fenzi et al*., 2012]. They all reproduce the cyclonic gyre of Prydz Bay and suggest a similar cyclonic circulation beneath the ice shelf (i.e., inflow of shelf waters in the east and outflow of Ice Shelf Water and marine ice formation in the west).

The occurrence of coastal polynyas within Prydz Bay plays a key role in the sea ice cycle. The Mackenzie polynya occurs in the western flank of the Amery calving front (Figure 1) and it is responsible for an average cumulative annual sea ice production of 68.2 $\pm$ 5.8 km^3 [*Tamura et al*., 2008]. The Barrier polynya occurs in the northeastern side of Prydz Bay, close to the shelf break, and it is responsible for an average cumulative annual sea ice production of 80.0 $\pm$ 19 km^3 [*Tamura et al*., 2008]. These polynyas are linked to the formation of High Salinity Shelf Water, whose role in the formation of Cape Darnley Bottom Water [*Ohshima et al*., 2013] is still under debate.

This paper discusses ocean observations measured beneath the ice shelf by an instrumented mooring in borehole AM02, together with new synchronous observations of the open ocean properties and current velocity along the eastern calving front of the AIS and augmented with CTD data from instrumented seals covering Prydz Bay. *Craven et al*. [2004] first documented the intrusion of relatively warm waters beneath the AIS from observations collected at the borehole site AM02 (Figure 1). This paper expands on the results presented in *Craven et al*. [2004] and, in particular, documents the spatial variability and seasonal inflow of mCDW. Estimates of basal melt beneath the AIS due to mCDW are presented for the first time, together with the interannual variability in heat content linked to mCDW. The circulation and seasonal cycle of the water masses observed at site AM02 are also described.

2. Data

Several data sets are used, extending from the AIS cavity to the open ocean north of the continental shelf break, offshore Prydz Bay. The latest bathymetry and the AIS cavity geometry characteristics are taken from the data set compiled by *Timmerman et al*. [2010], which is available from http://doi.pangaea.de/10.1594/PANGAEA.741917.

2.1. CTD and Mooring Survey

2.1.1. Boreholes

Borehole AM02 (69°42.8′S, 72°38.4′E) was hot water-drilled during the austral summer of 2000/2001. This site is located about 70 km southwest of the calving front, in a basal melt zone (Figure 1). At this site, the ice shelf is 373 m thick, the ice shelf base is at 326 dbar depth, and the water column thickness is 473 dbar [*Craven et al*., 2004]. Additional data are also used from borehole AM01 (69.443°S, 71.418°E), which is located approximately 100 km from the calving front of the AIS (Figure 1). At this site the ice shelf is 479 m thick, of which the deepest 203 m is accreted marine ice [*Morgan*, 1972].

Immediately after the hot water drilling and before the deployment of the mooring at site AM02, a series of CTD profiles were obtained from the ocean water column using a Falmouth Scientific (FSI) 3″ microCTD (serial 1610). Manufacturer calibration coefficients were applied prior to deployment. Because of the difficulty in retrieving calibration water samples from AM02, the FSI microCTD was compared against a General Oceanics Mark III CTD serial 1193 in two CTD casts aboard the RSV *Aurora Australis* shortly after the AM02 CTD profiles were measured. Four good CTD profiles from the borehole were retrieved over 5 days. Final FSI data accuracy estimates are as follows: temperature ~0.005°C, salinity ~0.03 (PSS78), and pressure ~2 dbar. An additional seven CTD profiles are also available from borehole site AM01 [*Herraiz-Borreguero et al*., 2013].

Table 1. Details of Mooring Deployments Within the Water Column at Borehole AM02

	Deployment Date	Mean Deployed Pressure (dbar)	Distance from the Ice Shelf Base (m)	Measurements	Time Series Coverage
Top	09/Jan/2001	338.5	12	T, S, P	2001, 2003–2006
Middle	09/Jan/2001	561	273	T, S, P	2001, 2003–2006
Bottom	09/Jan/2001	770	444	T, P	2001, 2003–2006
Bottom	09/Jan/2001	770	444	S	2001, 2003

After CTD profiling, a mooring was deployed through the ice shelf into the ocean cavity. The moorings consisted of three Seabird SBE MicroCATs (fixed at different depths) measuring temperature, salinity, and pressure at 30 min intervals. Manufacturer-supplied calibrations were applied internally by the MicroCATs, and calibrated data were output, with initial accuracies of 0.002°C for temperature, 0.003 (PSS78) for salinity, and 2 dbar for pressure. Table 1 summarizes the instrument deployments and the data retrieved per year. The deployment depths were chosen to be within ∼20 m of the ice shelf base, in the middle of the water column and within 20–50 m of the bottom of the water column.

2.1.2. Along the Ice Shelf Front

An array of moorings was deployed to study ice shelf-ocean interactions and a ship-based summer CTD survey was made along the calving front in February 2001 (Figure 1). The easternmost moorings, hereafter called PBM1 to PBM3, captured the seasonality of inflowing mCDW during 2001. Table 2 shows the design of each mooring (type of instrument, depth, and parameters measured). The whole array of moorings deployed at the ice shelf calving front is fully discussed elsewhere in a future publication. Here PBM1–3 are used to support the interpretation of the observations from the subice shelf mooring AM02. These records are concurrent with the first year of records at borehole site AM02.

2.2. Instrumented Elephant Seals

Over the last decade, southern elephant seals (*Mirounga leonine*) have been instrumented with Conductivity-Temperature-Depth and Satellite-Relayed Data Loggers (CTD-SRDLs), measuring vertical profiles of temperature (T) and salinity (S) during their foraging trips [*Fedak et al.*, 2004]. In the Indian Ocean, regular seals tagging has occurred every year since 2004 in the Kerguelen Islands, and on the Antarctic

Table 2. PBM Moorings 1–3 Instrumental Design[a]

Mooring (PBM)	Latitude (°S)	Longitude (°E)	Ocean Depth (m)	Instrument	Parameter Measured	Recording Interval	Instrument Depth (m)
PBM1	69° 22.014′	74° 38. 153′	750	RCM8	SPD, DIR, T, P	60 minutes	367
				MicroCAT	T, C	5 minutes	368
				RCM8	SPD, DIR, T, P	60 minutes	459
				MicroCAT	T, C	5 minutes	460
				RCM8	SPD, DIR, T, P	60 minutes	571
				MicroCAT	T, C	5 minutes	572
				MicroCAT	T, C	5 minutes	725
				RCM5	SPD, DIR, T, P	60 minutes	735
PBM2	69° 12.001′	74 05.962′	672	RCM8	SPD, DIR, T, P	60 minutes	370
				MicroCAT	T, C	5 minutes	371
				RCM8	SPD, DIR, T, P	60 minutes	462
				MicroCAT	T, C	5 minutes	463
				MicroCAT	T, C	5 minutes	647
				RCM8	SPD, DIR, T, P	60 minutes	657
				SBE39	T	5 minutes	324
PBM3	68° 52.386′	73° 33.310′	768	RCM8	SPD, DIR, T, P	60 minutes	347
				MicroCAT	T, C	5 minutes	348
				RCM8	SPD, DIR, T, P	60 minutes	439
				MicroCAT	T, C	5 minutes	440
				RCM8	SPD, DIR, T, P	60 minutes	551
				MicroCAT	T, C	5 minutes	552
				RCM8	SPD, DIR, T, P	60 minutes	663
				MicroCAT	T, C	5 minutes	664
				MicroCAT	T,C	5 minutes	743
				RCM8	SPD, DIR, T, P	60 minutes	753

[a]Instrument types used: SeaBird SBE37SM MicroCAT, SeaBird SBE39 and Aanderaa RCM current meter. For parameters, T = temperature, C = conductivity, SPD = current speed, DIR = current direction.

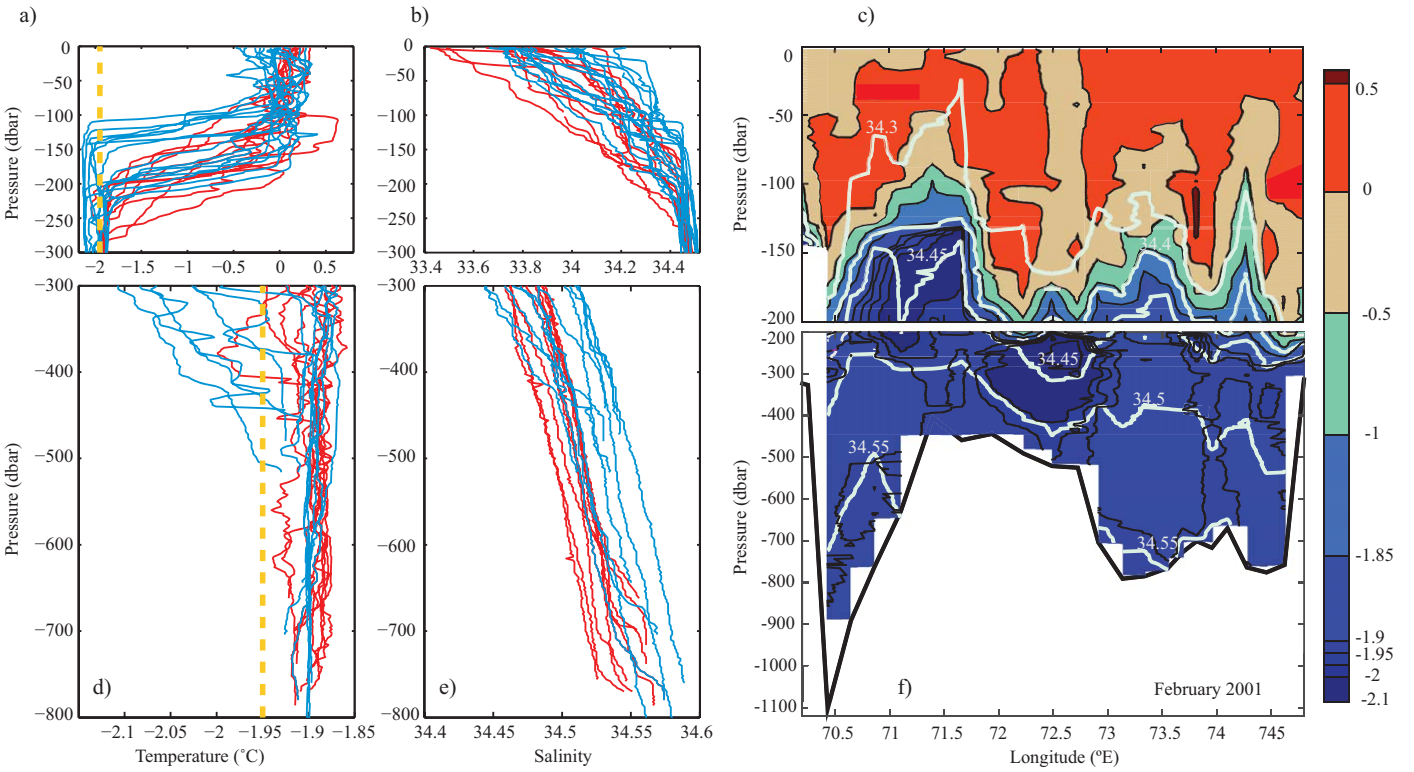

Figure 2. (a) Potential temperature and (b) salinity profiles, and (c) section, along the Amery Ice Shelf calving front during February 2001. Profiles east of 73°E are shown in red, while profiles west of 73°E are shown in blue. The yellow dashed line in Figure 2a is at −1.95°C. Salinity in Figure 2c is shown by white contours and temperature by the color scale.

continent from two of the Australian Antarctic stations, Davis and Casey in 2011, 2012, and 2013. Here we use a subset of data (∼16,000 T, S profiles) from Prydz Bay (*Roquet et al.*, 2014) and the AIS calving front vicinity to document the properties and spatial variability of CDW and mCDW in Prydz Bay, and how they relate to the observed mCDW in the ice shelf cavity. This subset of data extends from 55°S to the AIS calving front, and from 68°E to 82°E, during 2011–2013.

3. Results

3.1. Spatial and Temporal Variability of Water Masses Off the AIS

3.1.1. Spatial Variability at the Ice Shelf Calving Front

From the 2001 austral summer hydrographic section (Figure 2), the warmest water along the calving front is observed in the seasonal mixed layer, with no mCDW present during February 2001. The properties of the water column along the AIS calving front vary from west to east. A summer mixed layer is observed along the ice shelf front, deepening from west to east and with a maximum depth of 100–200 m (Figures 2a and 2b). The temperature of the mixed layer ranges from −0.3 to 0.3°C, with salinities from 33.4 to 34.3. While the mixed layer is more clearly observed in the temperature profiles, the salinity shows a step-like mixed layer, caused by mixing with sea ice meltwater (Figures 2a and 2b). The temperature and salinity variability observed in the summer mixed layer is dominated by mesoscale eddies, bringing warmer waters toward the ice shelf (Figure 2c). At least four eddies are easily distinguished, which extend well beyond the depth of the mixed layer (Figure 2c, at 74°E).

Below the mixed layer, the properties of the water column show similar zonal contrast as that at shallower depths (Figures 2d and 2e). Two water masses are found below the summer mixed layer: Ice Shelf Water (ISW) in the west, and High Salinity Shelf Water (HSSW) at bottom depths. Here we use water cooler than −1.95°C to define the core of the ISW plume and to better isolate the ISW plume. In the west, two ISW plumes are observed (Figure 2f), just below the summer mixed layer. The shallower plume, centered at ∼71°E, is found between 100 and 300 dbar, with a temperature between −1.95 and −2°C. The top 100 m of this ISW plume is at/below the in situ pressure freezing point. A deeper and larger ISW plume is observed

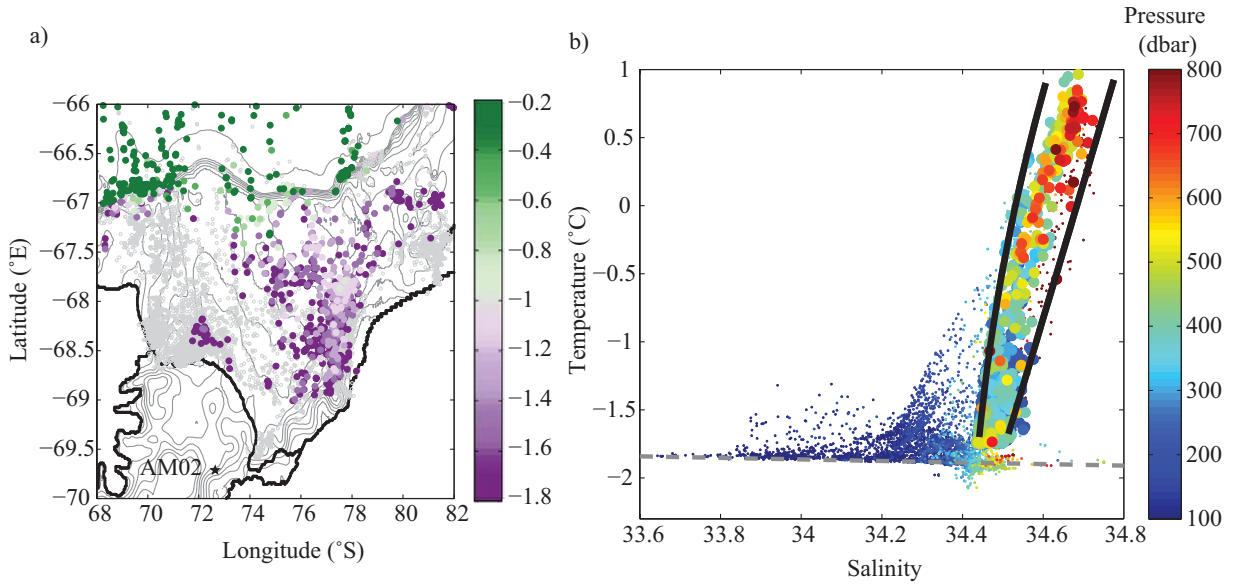

Figure 3. Modified CDW properties and spatial distribution during April and May retrieved by instrumented Elephant seals during 2011, 2012, and 2013. (a) Spatial distribution of the temperature of the mCDW core. Gray dots show the profiles without mCDW. (b) Temperature and salinity diagram of all the profiles shown in Figure 3a. MCDW is highlighted with larger markers. Colors show the pressure at which the potential temperature and salinity pairs were measured within the profile. Black thick lines show the 28.0 and 28.27 kg m^{-3} neutral density (γ^n) isopycnals. The gray dashed line shows the freezing temperature at the surface.

between 71.7°E and 73°E. In contrast, in the east, ISW is only observed at a couple of hydrographic stations (at ∼74.5°E, 350 dbar).

HSSW is the dominant shelf water mass and forms in winter during the formation of sea ice. Here we define HSSW as a layer with temperature between −1.85 and −1.95°C, and a salinity higher than 34.5 (potential density >27.75 kg m^{-3}). In front of the ice shelf, HSSW forms a thick isothermal layer between ∼400 m and the bottom. HSSW, formed by the Mackenzie polynya on the western flank of the calving front, occupies a thicker layer than observed in the east. The Mackenzie polynya overlies a deep depression (700–1200 m deep with a diameter of ∼10 km), which is isolated from the rest of Prydz Bay below depths of about 700 m (Figure 1). This allows HSSW to accumulate in this area, forming the thick HSSW layer observed almost throughout the year according to observations from mooring PBM7 (not shown). The salinity of the eastern HSSW (S < 34.55) is slightly fresher than the western HSSW (S > 34.55) (Figure 2e). The temperature of HSSW is slightly cooler than the surface freezing temperature (∼−1.89°C), suggesting mixing with ISW has occurred. While HSSW can also form at the Barrier polynya, the shallow bathymetry between the Barrier polynya and the Amery Depression (Figure 1) likely restricts the flow of this HSSW into Prydz Bay, at least during the summer months when we have observations and the volume of HSSW in the shelf break has declined.

A priori, it is expected that mCDW entering Prydz Bay would be directed toward the eastern flank of the AIS calving front, following the cyclonic gyre first described by *Smith et al*. [1984]. Indeed, modified CDW is observed almost exclusively in the eastern side of Prydz Bay (Figure 3a). We define the core of mCDW as the temperature maximum below 200 dbar with a potential density between 27.72 and 27.85 kg m^{-3} (28.0 < neutral density (γ^n) < 28.27 kg m^{-3}). The mCDW properties shown in Figure 3 correspond to April and May, since these are the months with the highest coverage by the instrumented seals across Prydz Bay. North of the continental shelf break, mCDW has a maximum temperature close to 0°C and salinity higher than 34.65 (Figure 3a). In contrast, only heavily modified CDW is present over the continental shelf. The depth of the modified CDW core is between 250 and 450 dbar (Figure 3b) between ∼67°S and 68.5°S, descending to 500–600 dbar as it approaches the ice shelf calving front (not shown).

3.1.2. Seasonality of mCDW From Moorings

The seasonality of inflowing modified CDW was documented by the three moorings deployed along the ice shelf calving front during 2001 (Figure 1). Stations PBM1–3 show a similar seasonal cycle of modified CDW and thus, only the temperature and salinity recorded at PBM1 and at the bottom layer of PBM3 are shown in this paper (Figure 4).

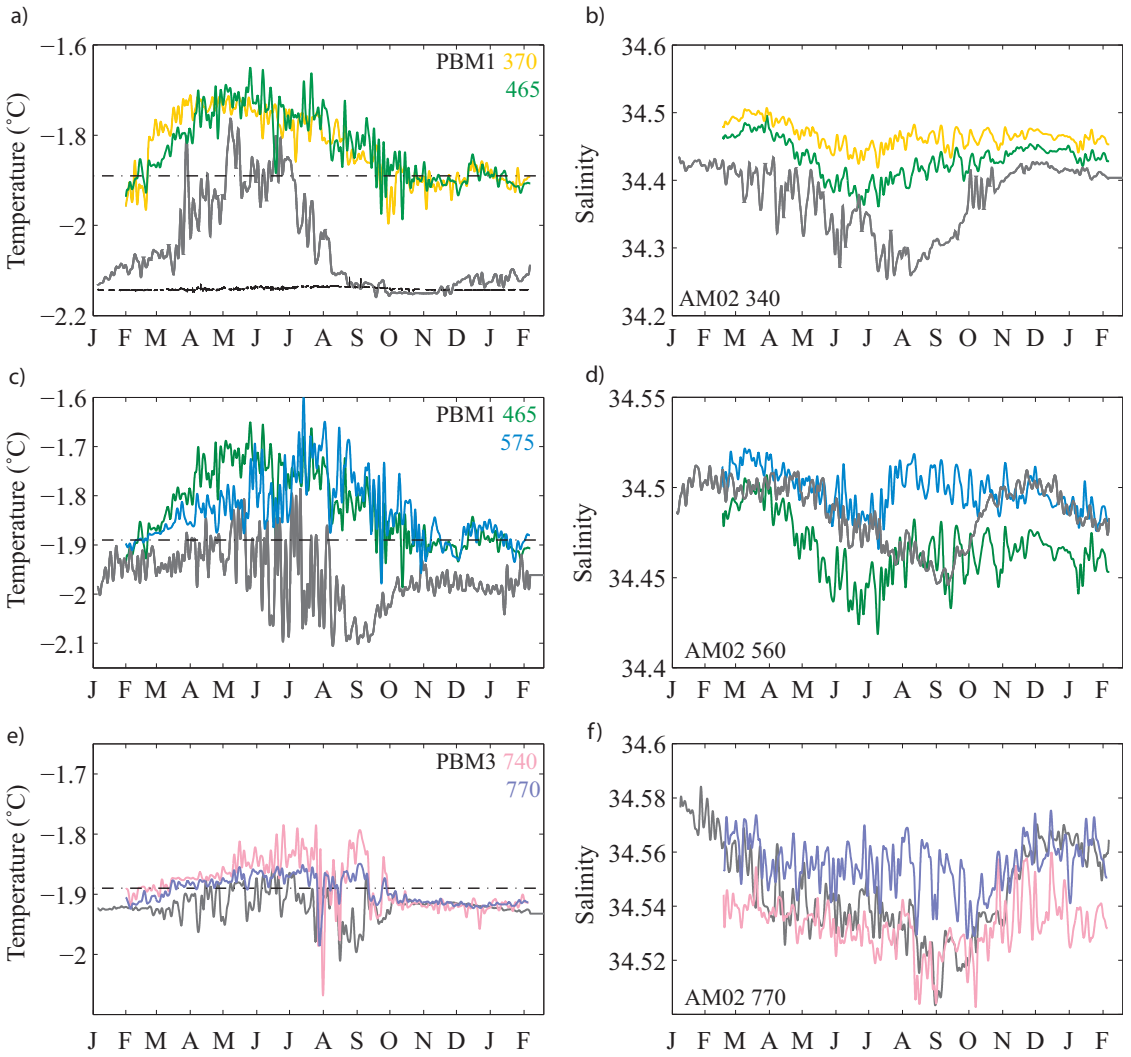

Figure 4. The 2001 (left) potential temperature and (right) salinity record at the eastern calving front and at ice shelf cavity site AM02. The calving front data are comprised of: PBM1 at 370 dbar (yellow), 465 dbar (green), and 575 dbar (blue); PBM3 at 740 dbar (pink) and 770 dbar (blue). The AM02 data at (a, b) 340, (c, d) 560, and (e, f) 770 dbar are shown in gray.

The presence of modified CDW was recorded below the depth of the summer mixed layer soon after the hydrographic section was completed. Modified CDW is first observed on the eastern flank of the Amery calving front by the end of February 2001 (Figure 5a, green and yellow), marking the onset of the temperature increase 12 m below the ice shelf base at site AM02 (Figure 4a, gray line). The highest mean temperature observed in the three PBM moorings along the ice shelf front ($\pm 1\ \sigma_{mean}$) peaks twice, at 330–465 dbar in May (-1.4 ± 0.1°C), with the highest temperature observed at PBM2 and PBM3 (not shown) and at 575 dbar in August (-1.53 ± 0.2°C). Beneath the ice shelf, the highest temperature (-1.7°C) peaks twice, in May and at the end of June (Figure 4a, gray).

3.2. Seasonal and Interannual Variability Beneath the Ice Shelf at AM02

To describe the seasonal cycle observed at AM02, a composite record for temperature and salinity was made using the complete 5 year record at all three depths (Table 1 and Figure 5). Comparison of the composite record to individual years allows us to distinguish between the mean 5 year seasonal cycle and interannual variability.

During the austral summer (November to March), relatively cold and saline ISW occupies the layer against the ice shelf base. Progressively warmer and fresher waters replace the ISW from March to late June. The

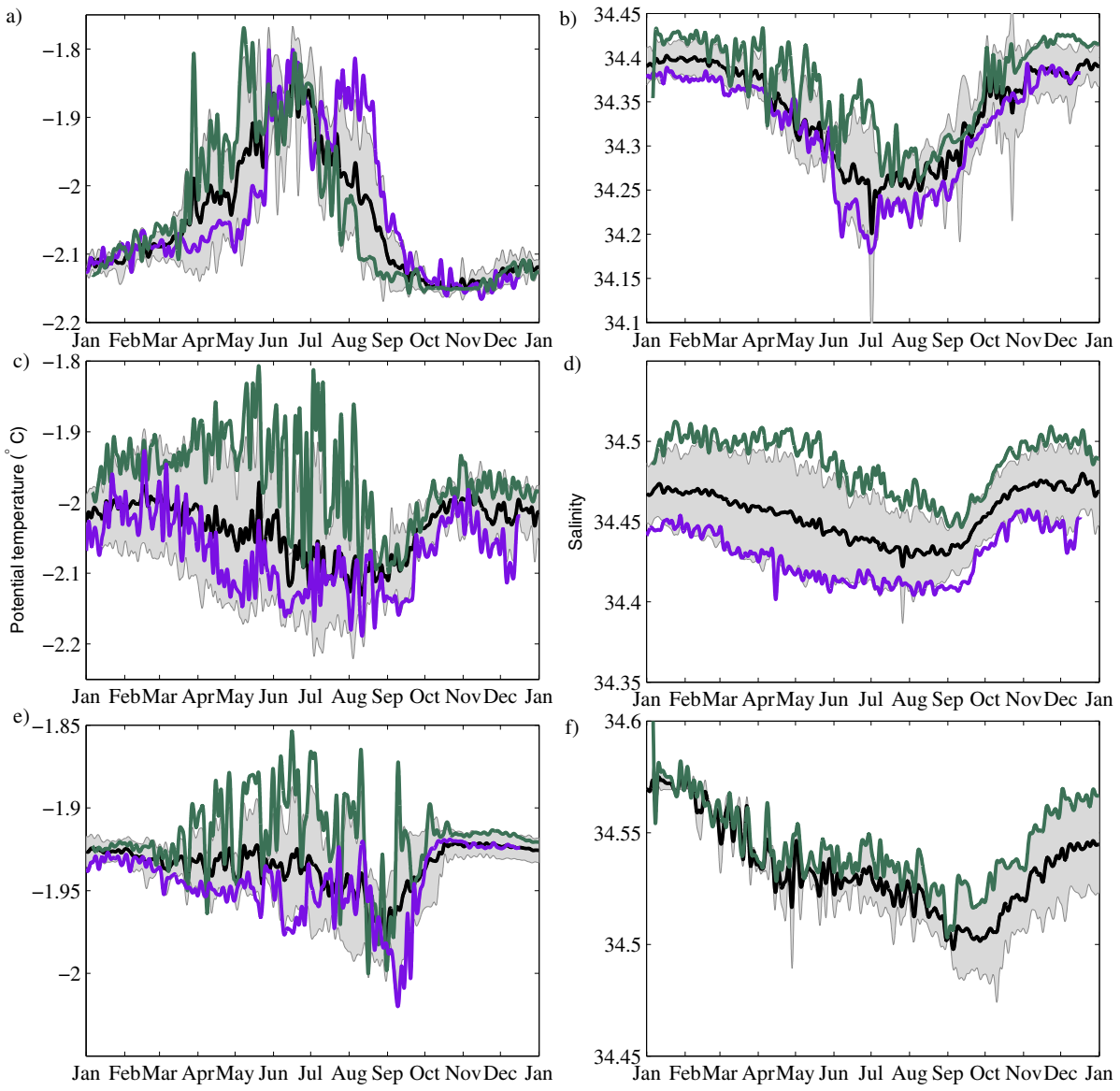

Figure 5. The composite records of (a, c, e) potential temperature (θ) and (b, d, f) salinity at AM02. The 40 h Butterworth filtered time series is shown as a thick line, with the $\pm 1\sigma$ (of the mean) shown as the thin line. Measurement levels are (a, b) 340 dbar, (c, d) 560 dbar, and (e, f) 770 dbar. The temperature and salinity during 2001 and 2006 are shown in green and purple, respectively. These have also been filtered using the 40 h Butterworth filter.

temperature peaks in late June, although the warmest temperatures can occur at other times between March and August (Figure 5a). Rapid cooling follows the peak in temperature, until the local pressure freezing point is reached by the end of the austral winter in late September. Salinity increases from July to November, at constant local freezing temperature, after which ISW properties are back to those observed during the austral summer. The ocean properties at mid and bottom depths show similar seasonality, but contrast with the top layer. From early spring (March) to winter (August–September), the mid and bottom layers cool and freshen, as observed at site AM01 [*Herraiz-Borreguero et al*., 2013]. This trend reverses in September, with relatively rapid increases in temperature and salinity restoring the initial austral summer characteristics (Figures 5c–5f).

Although understanding of the seasonal cycle is the main focus of this article, it is important to highlight the strong interannual variability observed in the inflow of mCDW. While the peak in ocean temperature occurs in late June in the mean, the timing of the arrival of mCDW varies from year to year. For example,

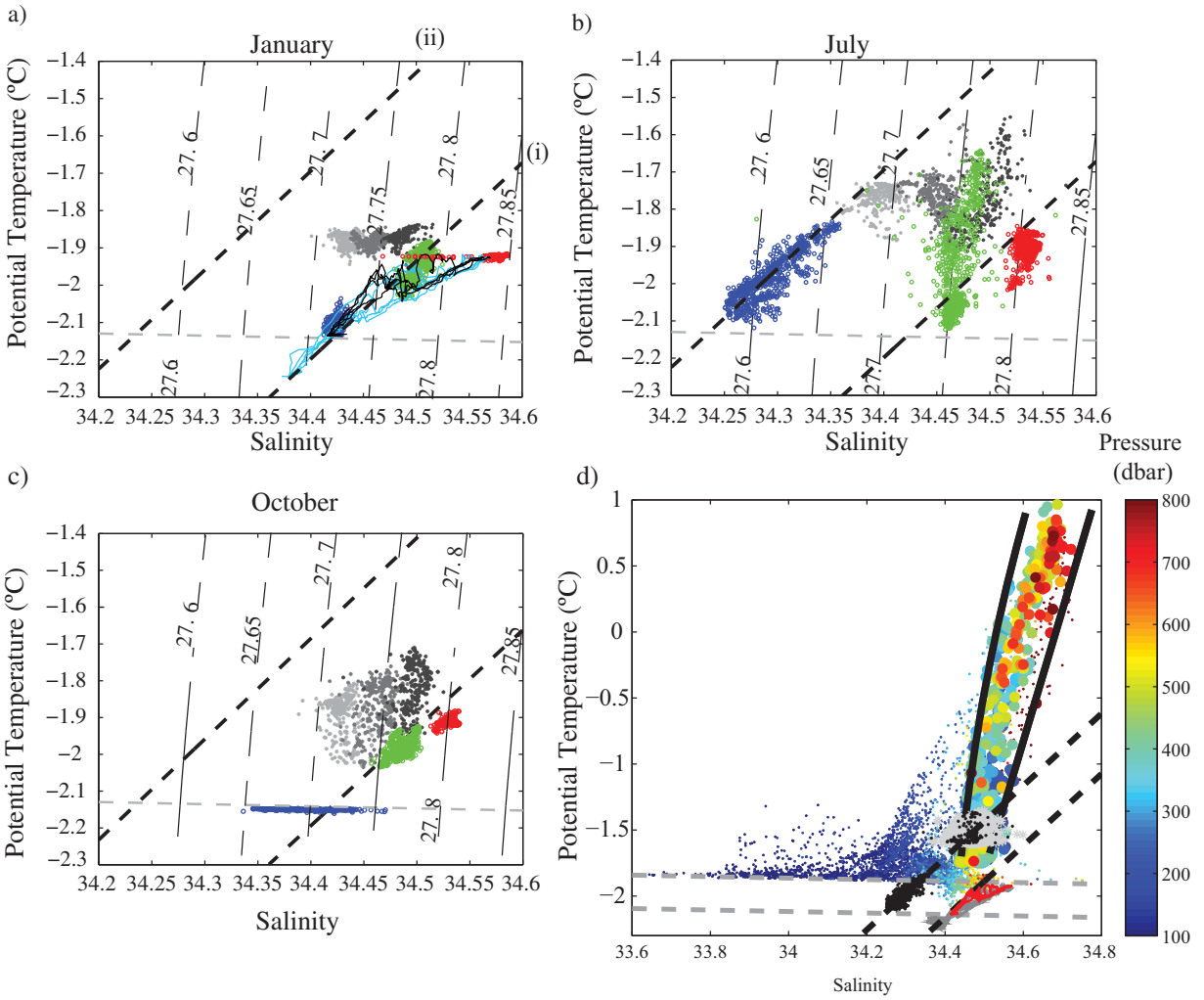

Figure 6. Potential temperature-salinity diagram, during (a) January and (b) July and (c) October. (d) Same as Figure 2b, with the maximum temperature observed above 370 dbar, at PMB1 (gray dots) and PBM3 (black dots), and the July temperature-salinity at 340 dbar at AM02. Data at AM02 are shown: navy blue (340 dbar), green (560 dbar), and red (770 dbar) dots. Summer CTD data at AM01 are shown in (a) light blue and (d) gray and at AM02 in (a) black and (d) red. At the calving front, only data at PBM1 is shown as gray dots, scaling from lighter (shallower) to darker (deeper) colors. Depths correspond to 370, 465, and 575 dbar. Two melt-freeze lines are shown as thick, black dashed lines. The in situ freezing temperature is shown as an almost horizontal gray dashed line.

the inflow of mCDW in 2006 was relatively late and produced two distinct temperature maxima (Figure 5a, purple). The arrival date of mCDW at AM02 varies between mid March and late May (Figure 5a), and lasts from 3–5 months. There seems to be a positive correlation between how early the inflow of mCDW is first observed at AM02, and its duration, with the exception of 2006 when a late inflow of mCDW persisted well into the winter (Table 3).

Table 3. Duration of the Inflow of mCDW As Observed at Site AM02—top MicroCAT

	March		April		May		June		July		August	
2001												
2003												
2004												
2005												
2006												

4. Discussion

4.1. Source Water for the Observed ISWs

Nøst and Foldvik [1994] showed that, to first order, ISW properties depend on the θ–S of the source water mass that produced it, hereafter source water, and are almost independent of

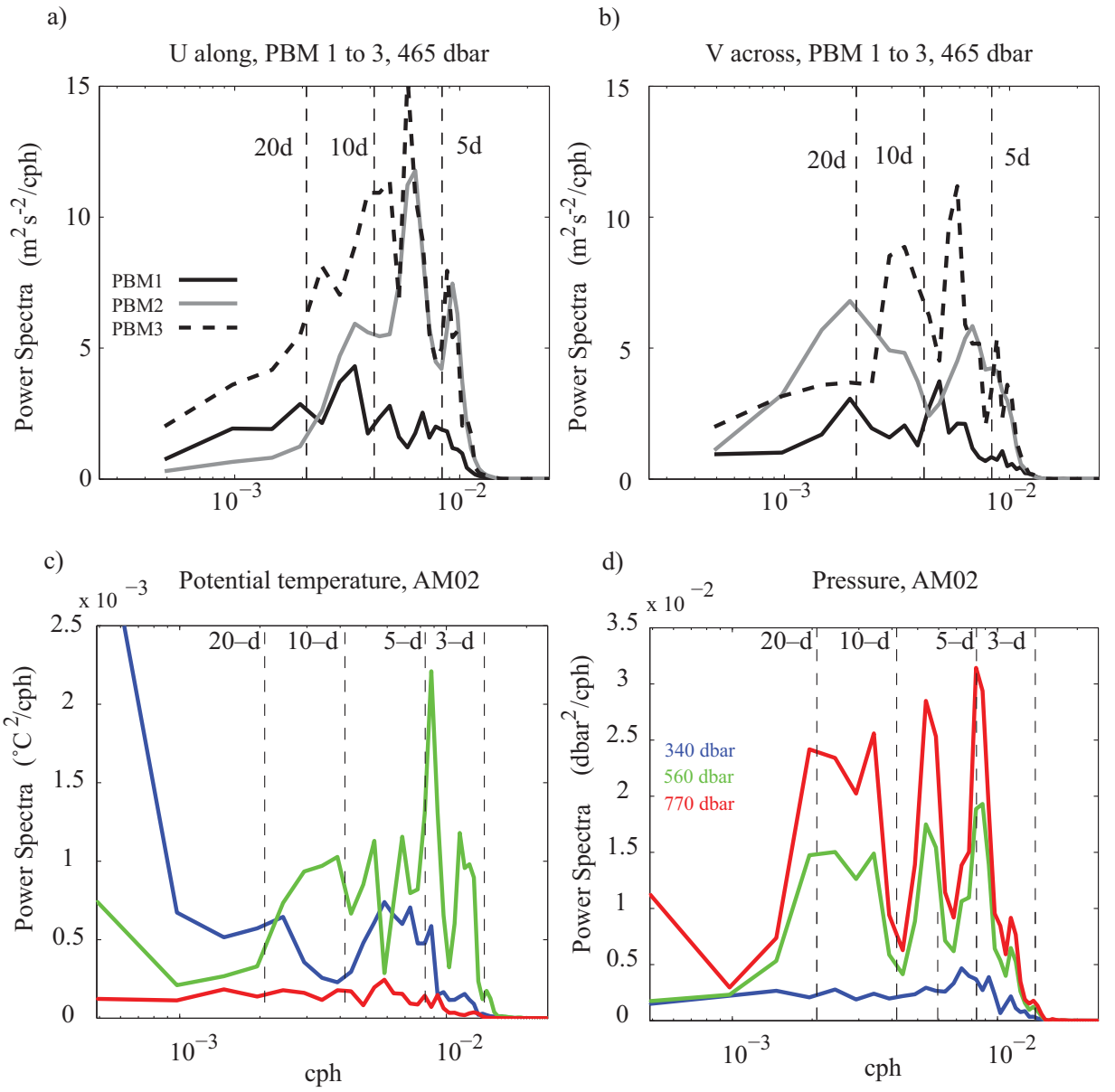

Figure 7. Spectral power of the (a) u-component and (b) v-component of the velocity measured at 465 dbar at PBM1–3, and of temperature and pressure at AM02 during 2001.

entrainment and melt rates. Thus, further mixing of ISW with its source water has little or no effect on the $\frac{d\theta}{dS}$ described by the Gade line [*Gade*, 1979]. The Gade line cannot be used to determine the θ–S of the source water from the ISW properties if mixing has occurred between varieties of ISW produced by source waters with differing salinities, or if ISW exits the cavity and its properties are modified by, e.g., atmospheric warming before reentering the cavity. We now discuss the possible source water mass of the ISW observed beneath the AIS, using the Gade line [*Gade*, 1979] to aid in our interpretation.

A key finding is the presence of two ISW types beneath the AIS, of independent water sources and seasonality. To explain the seasonal cycle and the origin of the two ISW types, we plot the temperature and salinity observed at PBM1 together with those observed at AM02 in Figure 6. The summer CTD profiles retrieved from AM01 and AM02 (Figure 1, gray stars) are also included (Figure 6a, cyan and black profiles, respectively). During the austral summer, the properties and features of the water column beneath the ice shelf at borehole sites AM01 and AM02 are fairly similar. In particular, the layer adjacent to the ice shelf base (Figures 6a–6c, blue dots) is occupied by ISW of similar characteristics to the ISW observed in the CTD profiles

at both sites. ISW at site AM01 is slightly cooler as the ice shelf draft here is ~100 m deeper than at site AM02.

The Gade line (i) in Figure 6 (or melt-freeze line) clearly shows that HSSW is the source water for this variety of ISW (hereafter, ISW_{HSSW}). From January to July, the mCDW observed at the ice shelf calving front (Figures 6a and 6b, gray dots) has reached AM02 and it is transformed into the ISW found in winter (Figure 6b, blue dots). This wintertime ISW is distinctly different to the ISW_{HSSW} (Figure 6d) and suggests that it is formed by a different water mass. The shallowest MicroCAT nicely captures the formation of this ISW: the mCDW observed at AM02 cools and freshens along the Gade line (ii), as it mixes with meltwater (Figure 6b, blue dots). The properties of the source water (θ_0 and S_0) used to draw the Gade line (ii) correspond to the mean θ and S of the warmest mCDW observed in the PBM1–3 (Figure 6d, gray and black dots). Hence, mCDW is the source water of this ISW (hereafter, ISW_{mCDW}).

A transition from (winter) ISW_{mCDW} to (summer) ISW_{HSSW} is observed from August to January, as the heat supply by mCDW is exhausted. In October, the temperature of the ISW_{mCDW} reaches the in situ freezing temperature (calculated at 370 dbar) (Figure 6, gray dashed line). This period of constant pressure freezing temperature is followed by a progressive salinity increase (Figure 6c, blue dots). The salinity increase is likely the effect of the mixing between both types of ISW. The ISW_{HSSW} replaces the lighter ISW_{mCDW} as the inflow of mCDW ceases (Figure 6c).

The salinity increase at constant freezing temperature at AM02 contrasts with the salinity increments observed at the borehole sites below the marine ice layer documented by *Herraiz-Borreguero et al*. [2013]. They showed that the salinity increments were episodic and linked to the presence of frazil ice. Moreover, the ISW properties did not evolve toward a distinct ISW as observed at AM02 (Figure 6c, blue dots). Nonetheless, episodic rapid increases in salinity are also observed at AM02 superimposed on the mean salinity trend, during October (e.g., Figure 4b, gray line). No marine ice layer is present at this site and so the salinity "spikes" are likely due to the formation of frazil ice rather than salt rejection from a marine ice layer.

The lighter ISW_{mCDW} has not been observed outside the subice shelf cavity yet. A possible fate could be that the fresher ISW_{mCDW} mixes with other water masses on its way out, becoming denser and even recirculating back into the ice shelf cavity. The deeper ice shelf draft at AM01 (~480 m) compared to AM02 (~373 m) is a barrier for the light ISW_{mCDW} observed at AM02 to reach AM01. Note that this ISW_{mCDW} is the lightest ISW observed in the ice shelf cavity and thus, being more buoyant will flow toward shallower drafts instead of deeper drafts as at AM01. Alternatively, this winter ISW exits primarily in the winter months where no observations are available and its signal is eroded by the convection resulting from sea ice formation.

4.2. Circulation of mCDW and Its Impact

The observations from site AM02 clearly show that modified CDW enters the ice shelf cavity. However, modeling studies reproducing the circulation beneath the AIS [e.g., *Williams et al*., 2001; *Galton-Fenzi et al*., 2012] do not show either the inflow of mCDW, or any basal melt associated with mCDW. Too much winter mixing, especially in the areas simulating the polynyas, may erode the mCDW completely during the austral winter.

The spatial distribution of mCDW revealed by the seal data (Figure 3) and the inflow of mCDW through moorings PBM1–3 agree very well with the inflow paths described by *Nunes Vaz and Lennon* [1996]. *Nunes Vaz and Lennon* [1996] also noted a secondary deeper inflow across the shelf break at the center of Prydz Bay, comprising a mixture of recirculated Prydz Bay waters and warmer CDW. Upwelling of CDW onto the continental shelf is thought to occur along troughs at the continental shelf break [e.g., *Walker et al*., 2007]. However, mCDW seems to enter Prydz Bay over the Four Ladies Bank (Figure 1), east of the deep trough of the Amery Depression. Similar southward flow of warm deep waters to the east of the Dotson trough has also been described in the central Amundsen Sea [*Ha et al*., 2014]. Recent observations using hydrographic profiles from seals have revealed the presence of two minima in dynamic height (not shown), which converge on the shallow Four Ladies Bank. The inferred circulation suggests that, in addition to the Prydz Bay gyre, there is a secondary clockwise recirculation to the east of the Four Ladies Bank and centered on the Barrier Bay polynya region (Figure 1). Both recirculations serve to draw mCDW onto the shelf in compensation for the outflow of dense shelf waters.

Eddy-driven flow may also be responsible for the inflow of mCDW into the AIS cavity. The westward deflection of the southeastward coastal current as it encounters the ice shelf front is likely to cause baroclinic

instabilities in the flow, allowing cross-frontal exchange with the ice shelf cavity. Eddies formed as a result of baroclinic instabilities are known to be responsible for the inflow of HSSW into the cavity of an ice shelf [*Årthun et al*., 2013; *Herraiz-Borreguero et al*., 2013]. These instabilities are linked to periods of 3–7 days, consistent with this study.

The eddy-like nature of the flow is supported by the power spectra of the v-component (across the ice shelf front) of the velocity at the eastern-most moorings PBM1–3 (Figure 7), which show peaks centered in the 3–7 day periods. A 2 day low-pass filter was applied to the velocity, temperature, and pressure prior to the calculation of the power spectra to remove any tidal signal. These periods are also observed in the power spectra of the temperature and pressure at site AM02 (Figure 7). Energy peaks are found at the 5 and 7 day period at the shallowest MicroCAT (Figures 7c and 7d, blue), and at 5 and 8 day peaks (both at T and P at intermediate depths). The inflow of mCDW is observed in the shallow and intermediate MicroCATs and their different spectra are likely due to the continuous modification of the mCDW into the fresher ISW at the upper most MicroCAT (e.g., Figure 6, blue dots), while the intermediate MicroCAT better reflects/represents the circulation (Figure 5c).

In the absence of velocity measurements under the ice shelf, the pressure measurements can provide some information about the nature of the flow. One can argue that the variability of the flow at the bottom of the water column would dominate any pressure variability in the upper MicroCATs, and indeed Figure 7d supports this argument. However, it also shows that the bottom layer is subject to similar forcing as the upper layers.

The seasonally variable inflow of mCDW and HSSW alter the vertical stratification in the ice shelf cavity. This change in stratification is best understood by comparing the salinities at the intermediate MicroCAT in AM02 (Figure 4d, gray line) with the salinities at the ice shelf calving front (Figure 4d, green and blue lines). Changes in salinity (and hence density) at a constant depth provide information about the vertical excursions of isopycnal layers. That is, a decrease in salinity throughout the water column reflects the deepening (or downwelling) of isopycnals and vice versa. Then, the overall freshening of the water column observed at the ice shelf front (Figure 4d, blue and green) from March to September translates into a downwelling of lighter isopycnals. This downwelling is clearly observed at AM02 from June to September (Figure 4d, gray line). As a result, mCDW can occupy a wider range of deeper depths. Indeed, mCDW is also observed below the ice shelf during these months and progressively at deeper levels (Figures 4a and 4c). This trend is interrupted in September, when the winter HSSW arrives at AM02 decreasing the temperature to the surface freezing point and increasing salinity as the sea ice formation season progresses (Figures 4d and 4f, gray line).

Similarly the inflow of HSSW results in the upwelling or shoaling of denser isopycnals at site AM02. This shoaling is nicely depicted by the temperature and salinity at the intermediate MicroCAT (Figures 5c and 5d) as a sharp increase in the salinity. The link between the timing of the respective mCDW and HSSW inflows is further supported by the strong correlation between the timing when HSSW arrives at AM01 and the exhaustion of mCDW inflow, that is, onset of the cooling following the temperature maximum linked to mCDW. They occur at the same time of the year. Interestingly, the densest HSSW at PBM3 is only observed during the austral summer months (Figures 6e and 6f), about 1 month after the arrival of HSSW is first observed at AM01 [*Herraiz-Borreguero et al*., 2013].

4.3. Ice Shelf Basal Melt Due to mCDW

Now that we have identified the source water for the observed winter ISW at AM02, we can calculate the mCDW heat flux and consequently, estimate the basal melt driven by mCDW. We begin by estimating the transport of mCDW through the array of moorings at the ice front by multiplying the area by the v-component of the velocity, after rotating into the along ice shelf flow direction. We calculate the transport of mCDW through the array of moorings at the ice front by multiplying the v-component of current velocity by the area of a vertical section centered around each of the 8 current meters on the PBM moorings. The typical width of these sections is 30 km, and the typical height is 100 m.

To test the likely role of mesoscale eddies in the transport of mCDW into the ice shelf cavity, we applied several low-pass Butterworth filters with periods of 2, 3, 5, and 7 days to the velocity. The annual mean transport of mCDW into the cavity varied considerably depending on the choice of the filter period. The

transport decreases by up to 40% depending on the filtering, supporting our claim that mesoscale eddies play an important role in driving the inflow of mCDW to the ice shelf cavity. Overall the strength and duration of eddies that enter the cavity is currently unknown, and the more conservative transport estimate of 0.22 ± 0.06 Sv (± 1 standard deviation), for a 5–7 day filter, is used to estimate the basal melt rate.

The annual melt rate is then estimated as

$$m = \frac{\rho F c_p (T_f - T) t}{\rho_i L A_i},$$

where ρ is ocean density (1027 kg m^{-3}), F is the mCDW flux into the ice shelf cavity (0.22 ± 0.06 Sv), c_p is the ocean heat capacity (4000 J kg^{-1} C^{-1}), T_f is the pressure freezing temperature at 345 dbar (the mean ice shelf draft for the area of the ice shelf base where mCDW can potentially drive basal melt), T is the temperature of the mCDW, t is the number of seconds in a year, ρ_i is the density of ice (920 kg m^{-3}), L is the latent heat of ice (334,000 J kg^{-1}), and A_i is the area of the ice shelf base where mCDW can potentially drive basal melt (12,773 km^2). This area is defined zonally by the eastern edge of the marine ice layer, following approximately the Fisher Glacier East flow line (Figure 1) and the easternmost grounding line, and meridionally by the calving front and the 500 dbar ice shelf draft. We have chosen 500 dbar because it is within the deepest depth at which mCDW has been observed at the calving front and within the cavity (Figure 5c). The temperature of mCDW, $T = -1.87°C$, is the mean temperature above $-1.95°C$, which marks the onset of the abrupt temperature increased observed at the shallowest instrument in AM02. Assuming that all the heat associated with this inflow is available for melt, it would result in total basal melt of 23.9 ± 6.5 Gt/yr (for a flux of 0.22 ± 0.06 Sv). If this was evenly distributed over the area, A_i, it would amount to an average basal melt rate of 2.0 ± 0.5 m of ice per year. Our basal melt estimates are based on the oceanographic conditions during 2001, which corresponded to one of the warmest inflows observed at AM02 (below).

Our basal melt rate estimate agrees fairly well with the estimate of *Craven et al*. [2004]. Combining measurements from a string of thermistors across the ice shelf-ocean interface and summer CTDs, they estimated a net melt rate ranging from 0.5 to 2 m/yr. This basal melt was attributed to tidal pumping and seasonally warmer waters of the coastal current penetrating the front part of the ice shelf cavity to shallow depths [*Jenkins and Doake*, 1991; *Jacobs et al*., 1992]. However, our results suggest that a seasonal (austral autumn-early winter) inflow of mCDW is responsible for the melt rate and the fresher ISW observed at AM02. This inflow occurs at intermediate depths, and 200–400 m deeper than the ice shelf base at the calving front where most of the tidally induced basal melt occurs [*Jacobs et al*., 1992; *Joughin and Padman*, 2003].

The inflow of mCDW as observed in AM02 shows large interannual variability in the arrival and duration of the inflow (Table 3), and thus in the heat flux into the ice shelf cavity. The rate of melting at the ice base depends on how fast heat and salt can be transported across the boundary layer to the ice-ocean interface. This, in turn, depends on other factors that are difficult to measure, such as ice shelf base roughness, and tidal and ocean current speed, and turbulence (and thus, heat/salt gradients across the boundary layer). To first order, the temperature of the water mass in contact with the ice shelf essentially controls basal melt rates, and it is the easiest to directly measure. We do not have information on changes in transport across the calving front from year to year, but we can assess changes in ocean heat content potentially available to drive basal melt during each of the mCDW inflows in AM02. We estimate the heat content in a 12 m thick layer between the ice shelf draft and the shallowest MicroCAT after removing the in situ freezing temperature at the depth of the ice shelf base and integrated over the duration of the warm inflow (Table 3). The variability in the heat content, referenced to 2001, shows that the first 2 years of the time series, 2001 and 2003, are the warmest, with 2003 showing $\sim$20% more available heat than 2001. This heat is considerably smaller by $\sim -40\%$ during 2004 and 2005, and by $\sim -20\%$ in 2006. These results highlight the high interannual variability in the inflow of mCDW, as has also been documented in the Amundsen Sea [*Dutrieux et al*., 2014].

Our results show that intrusions of modified CDW reach the AIS cavity cause lower basal melt rates ($<$2 m/yr) when compared to warm regime ice shelves such as Pine Island Glacier (up to 33 m/yr) [*Jacobs et al*., 2011]. The interaction of the mCDW with the AIS also results in the formation of a distinct ISW in contrast with "warm" regime ice shelves where no ISW is formed. mCDW intrusions are not unique to Prydz Bay with similar intrusions along East Antarctica offshore from the Mertz Glacier Tongue [*Williams et al*., 2010] and

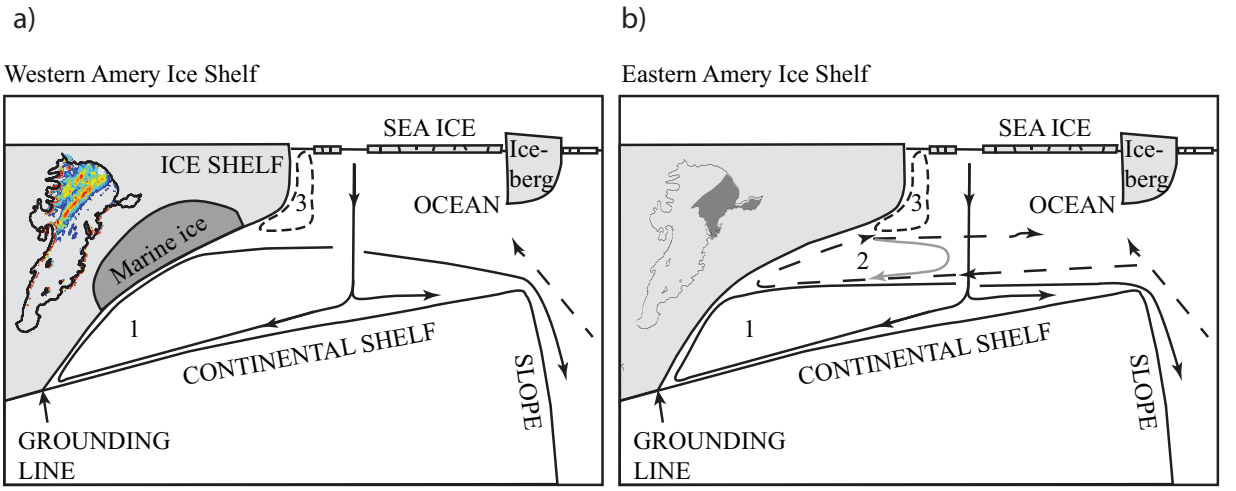

Figure 8. Schematic diagram of ocean circulation beneath the (a) western and (b) eastern Amery ice shelf in a vertical plane above the wide Antarctic continental shelf. Insets show (a) the thickness of accreted marine ice [*Fricker et al.*, 2001] and (b) assumed zone of basal melt due to mCDW. Vertical scale exaggeration ~1000/1. Numbers refer to ice-shelf basal melting modes described by *Jacobs et al.* [1992].

the Totten Glacier [*Williams et al.*, 2011]. These intrusions may reach the subice cavity and explain, at least, part of the high basal melt rates recently documented beneath several East Antarctic ice shelves [*Rignot et al.*, 2013]. Therefore, the impact of CDW over the East Antarctic ice shelves may be currently underestimated.

5. Conclusions

In this paper we examined the influence of mCDW intrusions on the ocean-ice shelf interactions of the AIS, primarily using time series from moored instruments deployed through boreholes. Two types of ISW are identified beneath the AIS, reflecting different source waters and mixing processes beneath the AIS. HSSW is the source water for the saltier ISW, which is formed during late winter-early spring, and occupies most of the ice shelf cavity. Contrary to prior modeling studies, mCDW reaches the AIS cavity, and results in a fresher ISW formed earlier during the austral winter. We estimate that in 2001 mCDW was responsible for a basal melt of up to 23.9 $\pm$ 6.5 Gt/yr (2.0 $\pm$ 0.5 m of ice per year). This basal melt could be up to 30% larger if mesoscale features are included in the mCDW influx. We expect strong interannual variability in this estimate corresponding to the variability in mCDW transport. The observations also suggest a strong relationship between the mCDW peak and the inflow of HSSW, which needs to be further explored to understand the high interannual variability observed in the inflow of mCDW and HSSW, and how these inflows may change in the future.

Our results show that the ocean circulation below the AIS is composed of two well-defined modes of circulation. These modes of circulation are depicted in Figure 8 following *Jacobs et al.*'s [1992] description of general two-dimensional ocean circulation below an ice shelf. In the western subice shelf cavity, the first mode comprises the inflow of HSSW and the formation of ISW and a marine ice layer [*Williams et al.*, 2001; *Galton-Fenzi et al.*, 2012; *Herraiz-Borreguero et al.*, 2013] (Figure 8a). In the eastern subice shelf cavity, the second mode comprises the inflow of mCDW at intermediate depths and formation of a fresher type of ISW (Figure 8b). This mode affects the outer eastern flank of the AIS and works in conjunction with the dominant HSSW mode (this one taking over when the inflow of mCDW is exhausted). The third mode depicted at the calving front occurs along the ice shelf front. Note that this depiction of the subice shelf circulation does not exclude zonal flows, but highlights the zonal contrast in the interaction of the ocean with the Amery Ice Shelf.

This work emphasizes the importance of austral winter observations both in the open ocean and beneath the ice shelves to fully capture the supply of ocean heat to the subice shelf environment; if we were limited to summer measurements, the key process driving mCDW-driven basal melt beneath the AIS would not have been observed. This is of critical importance and must be taken into account when designing programs for long-term monitoring of ice shelf-ocean interaction processes.

Acknowledgments
This work was supported by the Australian Government's Cooperative Research Centre Program through the Antarctic Climate and Ecosystems Cooperative Research Centre (ACE CRC) and by the Australian Department of Environment, CSIRO, and the Bureau of Meteorology through the Australian Climate Change Science Program. We acknowledge logistical support from the Australian Antarctic Division and the valuable input from the many people who have contributed to the AIS Ocean Research (AMISOR) ASAC1164 program. We thank Robin Muench and Alex Orsi for their valuable comments and discussions. Data from the boreholes and along the ice shelf front are available through the Australian Antarctic Data Centre (https://www1.data.antarctica.gov.au). The hydrographic data retrieved by the elephant seals are available from http://dx.doi.org/10/srk [*Roquet et al.*, 2014].

References

Allison, I. (1979), The mass budget of the Lambert Glacier drainage basin, Antarctica, *J. Glaciol.*, *22*(87), 223–235.
Årthun, M., P. R. Holland, K. W. Nicholls, and D. L. Feltham (2013), Eddy–driven exchange between the open ocean and a sub-ice shelf cavity, *J. Phys. Oceanogr.*, *43*(11), 2372–2387.
Clough, J. W., and B. L. Hansen (1979), The Ross Ice Shelf Project, *Science*, *203*(4379), 433–434, doi:10.1126/science.203.4379.433.
Craven, M., I. Allison, R. Brand, A. Elcheikh, J. Hunter, M. Hemer, and S. Donoghue (2004), Initial borehole results from the Amery Ice Shelf hot–water drilling Project, *Ann. Glaciol.*, *39*, 531–539, doi:10.3189/172756404781814311.
Depoorter, M. A., J. L. Bamber, J. A. Griggs, J. T. M. Lenaerts, S. R. M. Ligtenberg, M. R. van den Broeke, and G. Moholdt (2013), Calving fluxes and basal melt rates of Antarctic ice shelves, *Nature*, *502*, 89–92, doi:10.1038/nature12567.
Dupont, T. K., and R. B. Alley (2005), Assessment of the importance of ice-shelf buttressing to ice-sheet flow, *Geophys. Res. Lett.*, *32*, L04503, doi:10.1029/2004GL022024.
Dutrieux, P., J. De Rydt, A. Jenkins, P. R. Holland, H. K. Ha, S. H. Lee, and M. Schröder (2014), Strong sensitivity of pine island ice–shelf melting to climatic variability, *Science*, *343*(6167), 174–178.
Fedak, M. A. (2004), Marine mammals as platforms for oceanographic sampling: A "win/win" situation for biology and operational oceanography, *Mem. Natl. Inst. Polar Res.*, *58*, 133–147.
Foster, T. D. (1983), The temperature and salinity fine structure of the ocean under the Ross Ice Shelf, *J. Geophys. Res.*, *88*(C4), 2556–2564.
Fricker, H. A., S. Popov, I. Allison, and N. Young (2001), Distribution of marine ice beneath the Amery Ice Shelf, *Geophys. Res. Lett.*, *28*(11), 2241–2244.
Gade, H. G. (1979), Melting of ice in sea water: A primitive model with application to the Antarctic ice shelf and icebergs, *J. Phys. Oceanogr.*, *9*, 189–198, doi:10.1175/1520-0485(1979).
Galton-Fenzi, B. K., J. R. Hunter, R. Coleman, S. J. Marsland, and R. C. Warner (2012), Modeling the basal melting and marine ice accretion of the Amery Ice Shelf, *J. Geophys. Res.*, *117*, C09031.
Ha, H. K., A. K. Wåhlin, T. W. Kim, S. H. Lee, J. H. Lee, H. J. Lee, and O. Kalén (2014), Circulation and modification of warm deep water on the central Amundsen Shelf, *J. Phys. Oceanogr.*, *44*(5), 1493–1501.
Herraiz-Borreguero, L., I. Allison, M. Craven, K. W. Nicholls, and M. A. Rosenberg (2013), Ice shelf/ocean interactions under the Amery Ice Shelf: Seasonal variability and its effect on marine ice formation, *J. Geophys. Res. Oceans*, *118*, 7117–7131, doi:10.1002/2013JC009158.
Jacobs, S. S., A. L. Gordon, and J. L. Ardai Jr. (1979), Circulation and melting beneath the Ross Ice Shelf, *Science*, *203*, 439–443, doi:10.1126/science.203.4379.439.
Jacobs, S. S., H. Hellmer, C. S. M. Doake, A. Jenkins, and R. Frolich (1992), Melting of ice shelves and the mass balance of Antarctica, *J. Glaciol.*, *38*(130), 375–387.
Jacobs, S. S., A. Jenkins, C. F. Giulivi, and P. Dutrieux (2011), Stronger ocean circulation and increased melting under Pine Island Glacier Ice Shelf, *Nat. Geosci.*, *4*, 519–523, doi:10.1038/ngeo1188.
Jenkins, A., and C. S. M. Doake (1991), Ice–ocean interaction on Ronne Ice Shelf, Antarctica, *J. Geophys. Res.*, *96*(C1), 791–813.
Jenkins, A., and S. S. Jacobs (2008), Circulation and melting beneath George VI Ice Shelf, Antarctica, *J. Geophys. Res.*, *113*, C04013, doi:10.1029/2007JC004449.
Joughin, I., and L. Padman (2003), Melting and freezing beneath Filchner-Ronne Ice Shelf, Antarctica, *Geophys. Res. Lett.*, *30*(9), 1477, doi:10.1029/2003GL016941.
Morgan, V. (1972), Oxygen isotope evidence for bottom freezing on the Amery Ice Shelf, *Nature*, *238*(5364), 393–394.
Nicholls, K. W., and A. Jenkins (1993), Temperature and salinity beneath Ronne Ice Shelf, Antarctica, *J. Geophys. Res.*, *98*(C12), 22,553–22,568, doi:10.1029/93JC02601.
Nøst, O., and A. Foldvik (1994), A model of ice shelf–ocean interaction with application to the Filcher–Ronne and Ross Ice Shelves, *J. Geophys. Res.*, *99*(C7), 14,243–14,254.
Nunes Vaz, R. A., and G. W. Lennon (1996), Physical oceanography of the Prydz Bay region of Antarctic waters, *Deep Sea Res., Part I*, *43*(5), 603–641.
Ohshima, K. I., Y. Fukamachi, G. D. Williams, S. Nihashi, F. Roquet, Y. Kitade, and M. Wakatsuchi (2013), Antarctic Bottom Water production by intense sea-ice formation in the Cape Darnley polynya. *Nat. Geosci.*, *6*(3), 235–240.
Pritchard, H., S. Ligtenberg, H. Fricker, D. Vaughan, M. Van den Broeke, and L. Padman (2012), Antarctic ice–sheet loss driven by basal melting of ice shelves, *Nature*, *484*(7395), 502–505, doi:10.1038/nature10968.
Raup, B., T. Scambos, and T. Haran (2005), Topography of streaklines on an Antarctic ice shelf from photoclinometry applied to a single advanced land imager (ALI) image, IEEE Trans. *Geosci. Remote Sens.*, *43*(4), 736–742, doi:10.1109/TGRS.2005.843953.
Rignot, E., S. Jacobs, J. Mouginot, and B. Scheuchl (2013), Ice–shelf melting around Antarctica, *Science*, *341*(6143), 266–270.
Roquet, F., G. Williams, M. A. Hindell, R. Harcourt, C. McMahon, C. Guinet, and M. Fedak (2014), A Southern Indian Ocean database of hydrographic profiles obtained with instrumented elephant seals. Scientific Data, 1.
Scambos, T. A., J. A. Bohlander, C. U. Shuman, and P. Skvarca (2004), Glacier acceleration and thinning after ice shelf collapse in the Larsen B embayment, Antarctica, *Geophys. Res. Lett.*, *31*, L18402, doi:10.1029/2004GL020670.
Shepherd, A., D. Wingham, D. Wallis, K. Giles, S. Laxon, and A. V. Sundal (2010), Recent loss of floating ice and the consequent sea level contribution, *Geophys. Res. Lett.*, *37*, L13503, doi:10.1029/2010GL042496.
Smith, N. R., D. Zhaoqian, K. R. Kerry, and S. Wright (1984), Water masses and circulation in the region of Prydz Bay, Antarctica, *Deep Sea Res., Part A*, *31*(9), 1121–1147.
Tamura, T., K. I. Ohshima, and S. Nihashi (2008), Mapping of sea ice production for Antarctic coastal polynyas, *Geophys. Res. Lett.*, *35*, L07606, doi:10.1029/2007GL032903.
Timmermann, R., A. L. Brocq, T. Deen, E. Domack, P. Dutrieux, B. Galton-Fenzi, and W. H. F. Smith (2010), A consistent data set of Antarctic ice sheet topography, cavity geometry, and global bathymetry. *Earth System Science Data*, *2*(2), 261–273.
Walker, D. P., et al. (2007), Oceanic heat transport onto the Amundsen Sea shelf through a submarine glacial trough, *Geophys. Res. Lett.*, *34*, L02602, doi:10.1029/2006GL028154.
Williams, G. D., S. Aoki, S. S. Jacobs, S. R. Rintoul, T. Tamura, and N. L. Bindoff (2010), Antarctic bottom water from the Adélie and George V Land coast, East Antarctica (140–149°E), *J. Geophys. Res.*, *115*, C04027, doi:10.1029/2009JC005812.
Williams, G. D., A. J. S. Meijers, A. Poole, P. Mathiot, T. Tamura, and A. Klocker (2011), Late winter oceanography off the Sabrina and BANZARE coast (117–128°E), East Antarctica, *Deep Sea Res., Part II*, *58*(9), 1194–1210.
Williams, M. J., K. Grosfeld, R. C. Warner, R. Gerdes, and J. Determann (2001), Ocean circulation and ice–ocean interaction beneath the Amery Ice Shelf, Antarctica, *J. Geophys. Res.*, *106*(C10), 22,383–22,399.